Nanoscale

PAPER

View Article Online
View Journal | View Issue

Cite this: *Nanoscale*, 2022, **14**, 8753

Evaluating acid and metallic site proximity in Pt/γ-Al_2O_3–Cl bifunctional catalysts through an atomic scale geometrical model†

Ana T. F. Batista, *[a] Céline Chizallet, [a] Fabrice Diehl,[a] Anne-Lise Taleb,[a] Anne-Sophie Gay, [a] Ovidiu Ersen [b] and Pascal Raybaud *[a]

Quantifying the distances between metallic sites and acid sites is crucial for tuning the catalytic activity and selectivity of bifunctional catalysts involving sub-nanometric platinum (Pt) nano-particles (NP) highly dispersed on a chlorinated alumina support. Thanks to the quantitative use of high resolution scanning transmission electron microscopy in the high angle annular dark field mode, we first highlight the presence of few Pt NP together with Pt single atoms (SA) on γ-alumina supports exhibiting various morphologies (flat-like or egg-like), and chlorine (Cl) and Pt loadings. We demonstrate that increasing the Pt loading does not impact the NP sizes but only the Pt NP inter-distances, whereas the Cl loading influences the SA/NP proportion. Then, we establish a thorough geometrical model which accounts for the way in which the global average metallic – acid inter-site distances evolve from 1 nm to 6 nm as a function of three key physico-chemical descriptors: alumina morphologies, chlorine contents and size factor of alumina particles (directly linked to specific surface area). Considering that Cl is predominantly located at alumina crystallite edges, the morphology strongly impacts the Cl edge saturation: 0.4% for flat-like, and 1.2% for egg-like alumina at fixed specific surface area (~200 m^2 g^{-1}). At Cl edge saturation, the inter-site distance is found to be 3 nm for flat-like, and 1 nm for egg-like alumina. However, for fixed Cl loading, the inter-site distance is less discriminated by the morphology. We discuss these trends in the case of naphtha reforming catalysts and thanks to the as-obtained geometrical model, we identify the key alumina descriptors to tune the inter-site distance.

Received 14th January 2022,
Accepted 29th May 2022

DOI: 10.1039/d2nr00261b

rsc.li/nanoscale

1. Introduction

Metal-acid bifunctional catalysts have been of the upmost importance in industrial processes since the 1950s, when they were first developed for catalytic naphtha reforming. Since then their application has expanded to a myriad of industrial processes, the most acknowledged being hydrocracking, ranging from petroleum refining to upgrading alternative bio-sourced fuels and fine chemical synthesis.[1,2]

These catalysts feature noble metal (Pt, Pd) or transition metal sulfide (MoS_2) active phases with hydro-dehydrogenation functions and Brønsted acid active sites (present in zeolites, silica-aluminas or chlorinated aluminas) which catalyze isomerization as well as cracking. The mechanism for bifunctional transformations can be generally described by the following main steps:[3–5] (a) dehydrogenation of a saturated hydrocarbon to form an olefin on a metallic site; (b) skeletal rearrangement of the olefin on an acid site and possibly subsequent cracking; (c) (de)hydrogenation of the olefins resulting from step (b) on a metallic site. The tuning of the ratio of metal to acid sites in this type of catalyst is one key parameter for optimal performance. Indeed, a strong predominance of one function or the other will not only impair the bifunctional mechanism; it can also benefit monofunctional pathways. The description of the bifunctional mechanism above implies that the olefinic intermediates diffuse from one type of site to the other. If there are diffusional limitations at this level, the reaction rate is limited by the mass transport. This concept was first described by Weisz[5] in the form of an *intimacy criterion* which indicates the maximum distance between the metal and acid functions for which there is no mass transport inhibition. This is particularly critical for the mechanical mixtures of two monofunctional components that Weisz studied. When working with model molecule reactions and with catalysts in which the metal function has been impregnated directly of an

[a]*IFP Energies nouvelles, Rond-point de l'échangeur de Solaize, BP 3-69360 Solaize, France. E-mail: ana-teresa.fialho-batista@ifpen.fr, pascal.raybaud@ifpen.fr*
[b]*Institut de Physique et Chimie des Matériaux de Strasbourg, UMR 7504 CNRS-Université de Strasbourg, 23 rue du Loess 67034 Strasbourg Cedex 2, France*
† Electronic supplementary information (ESI) available. See DOI: **https://doi.org/10.1039/d2nr00261b**

acid support, diffusional limitations are not critical. Nevertheless, the concept of intimacy, proximity or distance between the two types of sites was maintained as a cornerstone of the study of bifunctionality, although moving away from its initial diffusion-focused meaning.

This is apparent in the criteria needed to achieve the "ideal bifunctional catalyst" (meaning of optimum activity and selectivity) as described by Guisnet:[6] (a) a high enough metal/acid ratio so that the acid function is rate limiting and (b) olefin intermediates undergo one single acid catalyzed transformation when diffusing from one metal site to the next. Point (b) is an expression of the distance between sites: Batalha *et al.*[7] found that the number of acid catalyzed steps is characteristic of the intimacy between metallic and acid sites in Pt/(Al_2O_3)-HBEA catalysts. The concept of ideal bifunctionality has been widely used in the study of hydroisomerisation and hydrocracking reactions, so that "ideal bifunctionality" and "ideal hydrocracking" are sometimes used interchangeably.[8] The model catalyst of Pt/zeolite or Pt/(Al_2O_3 + zeolite) is overwhelmingly used in bifunctionality studies and it has allowed for the two key parameters, metal/acid balance and inter-site distance, to be varied with relative ease. Progressively increasing the Pt loading increases the metal/acid balance.[7,9,10]

Different approaches have been taken to vary the distance between sites: mechanical mixtures of Pt/alumina + zeolite compared to alumina + Pt/zeolite;[9,10] selective impregnation of Pt on the alumina or on the zeolite component of a shaped Al_2O_3 + zeolite support (which is closer to industrial hydrocracking catalysts in which alumina is used as a binder in the support);[11,12] selective impregnation of Pt on special alumina/zeolite or silica-alumina composites designed at the nanoscale to result in different degrees of proximity.[8] Several of these studies suggest that the closest proximity (usually Pt/zeolite) is not necessarily the best for optimum selectivity,[11] indicating that the relative location of the active sites regarding one another is also important. However, the inter-site distance is not quantified in the majority of these works, it is inferred from the scale or size of the individual components (zeolite crystals, alumina crystallites, *etc.*), with the exception of Mendes *et al.*[13] which considered it to be half the distance between Pt nanoparticles calculated from their average distribution on the support volume.

Another class of bifunctional catalyst is the one used in catalytic naphtha reforming which aims at increasing the octane number of gasoline by dehydrocyclization reaction of linear alkanes into aromatic compounds.[14,15] The metallic active sites are located on ultra-dispersed platinum nanoparticles (NPs) or clusters. They activate dehydrogenation steps which are required in reforming conditions, but also undesired hydrogenolysis.[3,16,17] While high chlorine contents are known to enhance the Lewis acidity of alumina surfaces,[1,18] low chlorine doping (~1 wt%) enhances the Brønsted acidity of hydroxyl groups located on the alumina surfaces.[19,20] The latter catalyse isomerization, cyclization, and also undesired cracking steps. This chlorine promoting effect of Brønsted acidity was also reported for oxychlorination catalysts and revealed by CO-IR spectroscopy.[21] The way in which chlorine enhances Brønsted acidity of hydroxyl may originate from electronic effect through the Cl–Al–O(H) chemical bond network and from the modification of the hydrogen bond networks.[22–24]

For *n*-heptane reforming, model reaction for naphtha reforming, Said-Aizpuru *et al.* showed that the hydroisomerization selectivity follows a non-monotonous trend as a function of chlorine content and that the isomerization selectivity may also depend on the nature of alumina support.[25,26] This observation clearly calls for the need of establishing refined atomic scale descriptors of the catalyst's bifunctionality and to quantify more precisely the intimacy criterion.[27] Even if the intimacy criterion for mass transport is respected and there is adequate conversion it does not guarantee perfect selectivity. Indeed, the acid and metallic functions of commercial catalysts are balanced to tune their selectivity to a certain degree only: moderate acidity (chlorine content) to prevent cracking, small metal particles to prevent hydrogenolysis. However, what is not currently known and therefore cannot be tuned is the relative position of the active sites and distance between them which may govern the way in which degree intermediates are intercepted.

By contrast with zeolite based bifunctional catalysts, the location of the active sites (acid or metallic ones) remains highly challenging to define for catalytic reforming catalysts, hence the study of the intimacy criterion for these catalysts is currently limited. On the one hand, this limitation lies in the complex nature of the acid sites which results from the intricate effects of chlorine atoms and surface hydroxyls of alumina.[22] On the other hand, the metallic phase is constituted of sub-nanometric Pt aggregates highly dispersed on the alumina support.[28,29] Hence, due to the high degree of dispersion of both entities, it is highly challenging to evaluate unambiguously their relative distances by usual experimental techniques. In this context, our work aims at proposing geometric models on the basis of characterization of the metallic phase of a set of platinum catalysts supported on chlorinated γ-Al_2O_3, and of the recent knowledge obtained about the location of chlorine on alumina.

Indeed, significant progresses have been achieved on the understanding of atomic scale properties of model chlorinated alumina supported platinum active phase, which provided more quantitative descriptors on the acid and metallic sites. Thanks to the combination of *infra*-red (IR) analysis and density functional theory (DFT), it was possible to identify that monodentate hydroxyls of γ-alumina are preferentially exchanged by chlorine.[22] More recently, ^{1}H NMR and DFT have shown that those exchangeable hydroxyls exhibit a specific chemical shift close to 0 ppm and are located on the edges of the γ-alumina platelets.[30] Simultaneously, the impact of alumina platelet morphology, either flat or egg-like, on the chlorine edge/facet distribution was highlighted. This result will deserve our attention in our current investigation since it provides the first estimate of the specific location of chlorine atoms to be presumably associated with vicinal acid sites of

alumina. Regarding the metallic active phase, high-resolution imaging using high angle annular dark field in scanning transmission electron microscopy (HAADF-STEM) and tomographic analyses enabled to identify that ~70–78% of platinum nanoparticles (NP) of size ~0.9 nm, are located at the edges on the γ-alumina platelets (flat-type, only, 1.3 wt% chlorine) for two Pt loadings (0.3 wt% and 1 wt%).[29] Surprisingly, HAADF-STEM also revealed that ~20% of Pt atoms were present as single atoms (SA) which increases further the system's complexity. SA offered an exponentially growing interest in catalysis during the last decade.[31–36] Also, Pt SA sites located on alumina have been the subject of many experimental and theoretical investigations which revealed appealing catalytic properties[37,38] although their stability under reacting environment (in particular, reducing environment) is also questioned.[39–41] Interestingly, it was also reported by several experimental techniques such as H_2 chemisorption,[42] EXAFS,[43–45] and TEM[45] that chlorine favours the (re)dispersion of Pt nano-particles on alumina. It was also invoked that this redispersion phenomenon occurs through the formation of PtO_xCl_y mono-nuclear species.[42] It will be thus interesting to analyse if the proportion of Pt SA may also be influenced by the chlorine content of the alumina support.

The main goal of the present work will be thus to provide an improved quantification of acid site-metallic sites distance, a key but still poorly known descriptor, as a function of the alumina morphology (either flat or egg). For that purpose, we will build a thorough geometrical model able to include the effects of various physico-chemical parameters such as alumina morphology and chlorine loading. This will be possible by considering in particular our previous understanding on the respective locations of chlorine atoms and platinum NP, including edge effects.[29,30] As a starting point, we provide HR HAADF-STEM insights on Pt NP and Pt SA extending our previous study[29] to a larger set of well-defined chlorinated alumina supported Pt samples, varying platinum and chlorine loading as well as alumina support morphology (either flat or egg). A strong effect of chlorine content on the SA population and metal-acid site distance is revealed.

2. Experimental part

2.1. Catalyst preparation

Two gamma-alumina supports were obtained from commercial boehmite powders from Sasol: PuralSB3 (BET surface of 183 $m^2\ g^{-1}$ by N_2 physisorption) and TH100 (BET surface of 149 $m^2\ g^{-1}$). These two supports exhibit different morphology, as shown by TEM (Fig. S1†), and will be called P-egg (for PuralSB3) and T-flat (for TH100) as defined in our previous works.[29,30] Catalysts were prepared by diffusional impregnation of γ-Al_2O_3 extrudates prepared with a H_2PtCl_6 and HCl solution, followed by drying overnight and finally calcination at 520 °C for 2 h under dry air (heating 5 °C min^{-1}, 1 L min^{-1} $g_{cat}{}^{-1}$). For the 1.4% w/w Cl samples, the chlorine loading was increased by thermal treatment at 520 °C by adding dichloropropane ($C_3H_6Cl_2$) to the air flow in the proportion of 1 wt% per gram of catalyst, which decomposes into HCl, H_2O and CO_2, creating a HCl partial pressure that allows for the exchange of surface hydroxyls with HCl. For the 0.1% w/w Cl samples, the chlorine loading was decreased by dechlorination, by injecting 8000 ppm of water into a dry air flow (1 L min^{-1} $g_{cata.}{}^{-1}$) at 520 °C. The H_2O partial pressure shifts the surface species equilibria to form surface hydroxyls and gaseous HCl. Both of these chlorine loading tuning procedures are based on the same principle, that the chlorine coverage depends on HCl partial pressure at a given H_2O partial pressure.[22] The supported Pt species formed during the calcination in the presence of chlorine correspond to a $PtCl_xO_y$ species, as previously shown by EXAFS analysis.[29] These oxide catalysts were then reduced under H_2 flow at 500 °C for 2 h, after a 30 min pre-calcination at 520 °C under dry air (heating 5 °C min^{-1}, 1 L min^{-1} $g_{cat}{}^{-1}$). After reduction, we obtain reduced platinum species on the support as previously shown by EXAFS analysis for which Cl neighbors could not be fitted.[29] Two series of catalysts were prepared so as to have a platinum loading of 0.3% w/w or 1% w/w (measured for oxide samples by X-ray fluorescence). They are referred to as 0.3%Pt/γ-Al_2O_3–Cl and 1%Pt/γ-Al_2O_3–Cl, respectively (see ESI section 2† for detail).

2.2. Scanning transmission electron microscopy

High resolution high angle annular dark field in scanning transmission electron microscopy (HR-HAADF-STEM) imaging were carried out on a Cs-corrected JEOL JEM 2100F microscope, operated at 200 kV, equipped with a JEOL HAADF detector. The camera length used in the HAADF mode was 10 cm, corresponding to inner and outer diameters of the annular detector of 60 and 160 mrad, respectively. The size of the electron probe in STEM mode is 0.11 nm. Before the STEM analyses, the powdered samples were deposited without solvent on a 300 mesh holey carbon copper grid.

3. Results and discussion

3.1. Structural characteristics of nanoparticles (NP)

HAADF-STEM images of the reduced catalysts for the various chlorine and Pt loadings are presented in Fig. 1, S2 and S3.† After reduction, well defined and well dispersed platinum nanoparticles (NPs) can be observed. The NP size histograms and the corresponding average size (Fig. S2–S3 and Table S1,† respectively) reveal the same average NP size for all the catalysts, *i.e.* 0.9 nm, regardless of platinum or chlorine loading, and of alumina type. The histograms also show a narrow size distribution with 70% of the measured NPs' sizes being comprised between 0.6 and 1.2 nm. The synthesis and reduction protocols thus uniformly control NP size and guaranty high metal dispersion. This NP size is similar to those reported in previous works[46,47] for similar ranges of Pt loading. It can be discerned however that fewer NPs are present on the catalysts with 0.3%Pt loading. Indeed, it seems logic that, at constant NP size, less impregnated platinum will result in less numer-

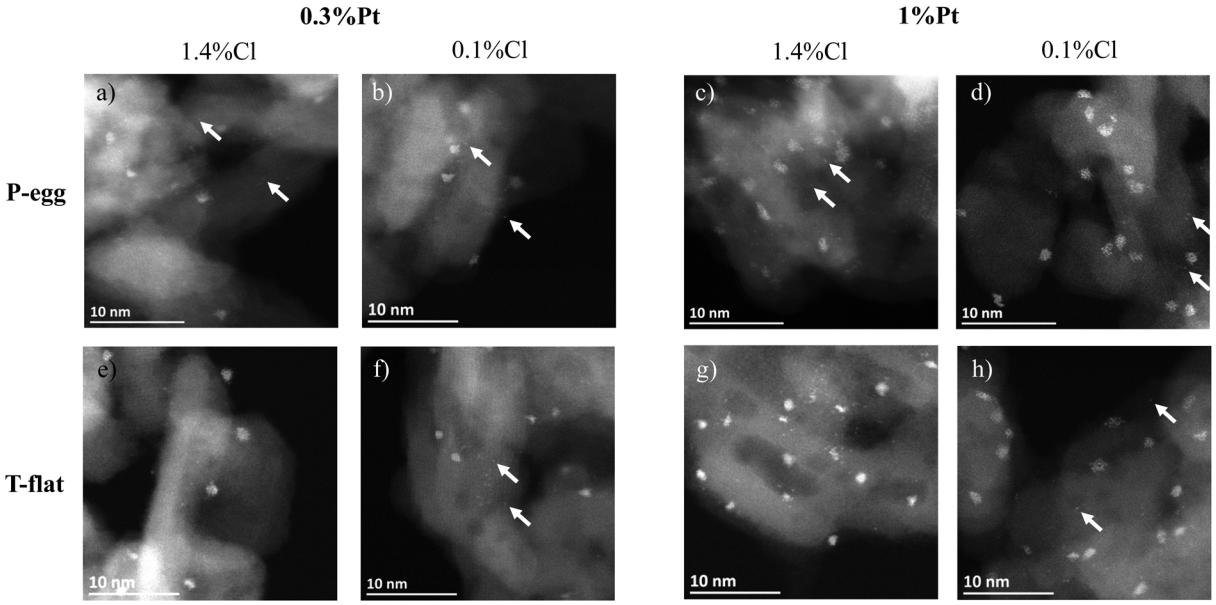

Fig. 1 HR-HAADF-STEM images of the reduced catalysts (a) to (d) on the P-egg support, (e) to (h) on the T-flat support, with 0.3%Pt (left, a–b–e–f) and 1%Pt (right, c–d–g–h) and 1.4%Cl (a–e–c–g) and 0.1%Cl (b–f–d–h). White arrows highlight single atoms. Figures (e) and (g) are from ref. 29 (with permission).

ous nanoparticles. It can be thus deduced that the average distance between platinum NPs will be larger for catalysts with 0.3%Pt loading than for those with 1%Pt, assuming that the NP distribution on the support is homogeneous as it is qualitatively highlighted in STEM images of Fig. 1.

Images acquired at higher magnification reveal that the NP structure is made of at most two layers of Pt atoms (see Fig. S4 in ESI section 1† for detail). This feature was observed for the whole set of samples investigated in the present work and can be assigned to a flat bi-planar morphology, often called "raft-like", which had already been suggested for this type of samples from microscopy,[46,48,49] XAS[49] and *ab initio* studies.[50,51] Overall, NPs are composed of 10 to 20 Pt atoms, which is compatible with the Pt_{13} nanoparticle model used in previous DFT studies.[50–52] DFT calculations[50] showed the bi-planar Pt_{13} morphology is the most stable on the dehydrated (100) alumina surface and a 3D morphology is the most stable on the (110) surface. The analysis of the image intensity suggests that 3D semi-spherical (or spherical) NPs are not present in our samples, as their center would appear with a higher intensity. Indeed, a follow up study[51] showed that the flat Pt_{13} morphology is not exclusive to the (100) alumina surface when it is stabilized by H and Cl migration.

3.2. Identification of single atoms

Thanks to the possibility to acquire high magnification images with a high signal-to-noise ratio, the presence of several single atoms was evidenced, as highlighted by white arrows in Fig. 1. The population of single atoms was quantified through the number of single atoms (SA) *vs.* number of nanoparticles (NP) ratio (#SA/#NP). For each catalyst, it was also possible to estimate the averaged ratios for three high enough magnification images. For each image, single atoms and nanoparticles were counted in the area of the image judged to be in focus. Imaging in STEM mode on an aberration corrected microscope has a very small depth of field and the same image may include regions with different heights. The consequence is a less optimal focus in some regions that is enough to prevent single atoms from being observed, even if the resolution is good enough to identify the nanoparticles.

According to the results presented in Fig. 2, several trends can be identified. Firstly, the proportion of single atoms is systematically lower for the samples at 0.1%Cl than at 1.4%Cl. Assuming that a NP is composed of 13 Pt atoms, the proportion of deposited platinum atoms present in the form of single atom varies from 10% up to 21%. This is an evidence of the stabilizing effect of chlorine on the smallest platinum species, particularly the single atoms, as predicted by DFT computational studies.[51]

Second, an impact of platinum loading on the #SA/#NP ratio for the 0.1%Cl samples is highlighted: the proportion of single atoms is smaller for the highest Pt loading on both supports. For 1%Pt, there is a higher absolute quantity of metallic entities for the same amount of chlorine (Pt/Cl $\approx$ 1 atom/atom), in comparison with the case at 0.3%Pt (Pt/Cl $\approx$ 0.5), resulting in a smaller proportion of single atoms. Thus, at 0.1%Cl, there is too little chlorine left to stabilize the single atoms. However, the impact of metal loading observed for the 0.1%Cl series is not observed at the highest chlorine content: for 1.4%Cl, the chlorine coverage seems to be high enough for stabilizing all the single atoms, whose proportion is mainly dictated by the chlorine content.

Lastly, it was observed that the type of alumina (P-egg *versus* T-flat) also has an impact on the #SA/#NP ratio as the

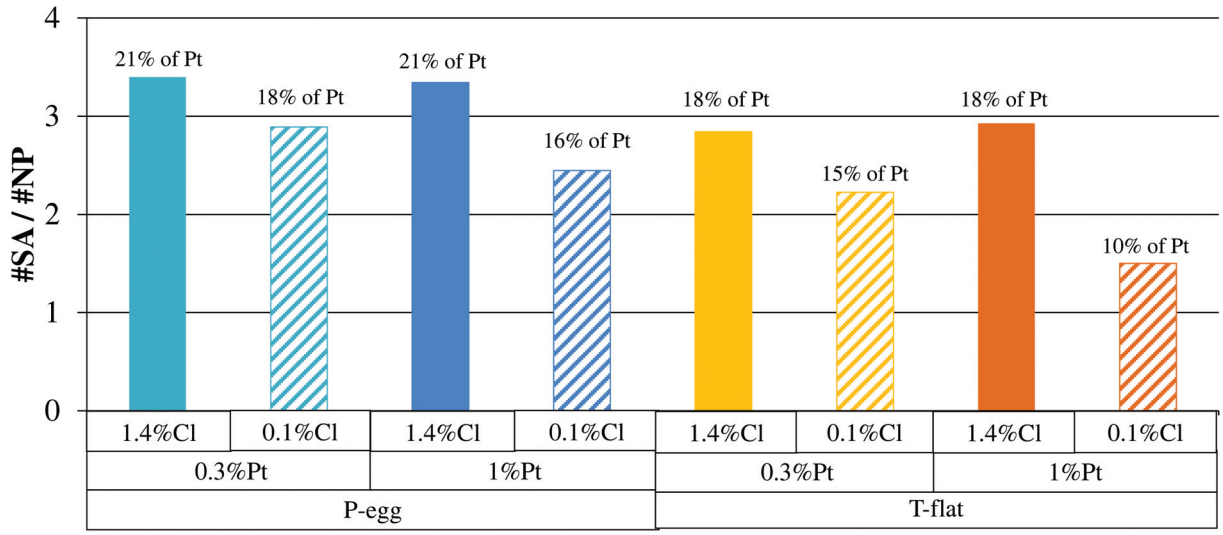

Fig. 2 Quantification of single atom population through #SA/#NP ratio and estimation of proportion of Pt as SA assuming that a NP is composed of 13 Pt atoms calculated for all reduced catalysts, and two Cl loadings: 1.4%Cl loading in full color and 0.1%Cl loading in stripes.

single atoms proportion is smaller for the catalysts supported on T-flat. This result seems to be the expression of a differing stabilization of platinum between the two supports. Since a previous NMR and DFT study showed that P-egg exhibits a higher edge/surface ratio than T-flat and that Cl is located at edges,[30] we may suggest that the more numerous chlorinated edge sites of P-egg may play a role in the stabilization of Pt SAC. Also, due to the larger surfaces exposed by T-flat, it may also be more difficult for Cl to migrate close to Pt due to larger distance/location.

3.3. Synopsis of the experimental observations obtained from STEM

Thus, as a synopsis of the findings from the STEM analysis reported herein and in our previous work,[29] it can be concluded that:

- All samples, supported on the T-flat and P-egg aluminas, from 0.3 to 1%Pt and from 0.1 to 1.4%Cl, exhibit similar platinum particle size distributions, with an average size close to 0.9 nm. For two of these samples (1%Pt/P-egg-0.1%Cl – present work – and 1%Pt/T-flat-1.4%Cl – our previous work[29]), a biplanar morphology of the NPs is observed.

- For two of these samples (0.3%Pt/T-flat-1.4%Cl and 1%Pt/T-flat-1.4%Cl – our previous work[29]), the majority (78%) of the particles are located on edges or defects of the alumina support. The tomography analysis needed to reach this conclusion can, however, not easily be transposed to the P-egg supported samples, due to the smaller crystallite size and much less defined edges of the latter with respect to T-flat. Considering the similarity of the size and morphology features exhibited by the particles in all the samples, it can be safely assumed that a vast majority of particles are also located on the numerous edges and defects of the P-egg support too.

- Single atoms exist in all samples, in a proportion that varies mainly with the chlorine content and the support morphology. High chlorine contents and edges (or defects) concentrations promote the presence of single atoms.

3.4. Geometric model of Pt/alumina-Cl catalysts

Based on our previous findings on the location of chlorine atoms[30] and of Pt NPs on the alumina support as summarized in section 3.3. (present work and ref. 29), a geometric model of the P-egg and T-flat based catalysts was built in order to estimate the distance between the two types of sites. This model should reflect, firstly, the surface to edge aspect characteristic of the crystallites of each alumina and, secondly, the preferred location of chlorine and of Pt NPs.

First, the model alumina platelets were chosen to reflect at best the surface to edge ratio of the supports crystallites and were inspired by the TEM study of their morphology.[30] They are represented in Fig. 3. For T-flat model platelet, a parallelepiped was chosen with main dimensions a, b and c. Based on the knowledge of alumina crystallite facet exposition found in the literature,[53–56] such a parallelepipedic platelet would expose (110) and (100) facets. For P-egg, a rhombicuboctahedron of edge length a was chosen. This polyhedron morphology is actually built from a perfect spinel type $MgAl_2O_4$ bulk structure, of which crystallites expose the (110), (100) and (111) terminations in the following proportions, 55.9%, 28.0% and 16.1% respectively. It can be described as two square copulas assembled on an octagonal prism. Note that these are simplified models of the platelet morphology, as can be evidenced from our previous work.[30] A parallelepipedic platelet does not expose the (111) facet, which was found to be present for both T-flat and P-egg. Also, in the case of P-egg, it's crystallites exhibit a more elongated or oval shape than that of the rhombicuboctahedron.

To validate these model platelets, a series of parameters were calculated and compared to those experimentally deduced from the analysis of our samples. Note that the stack-

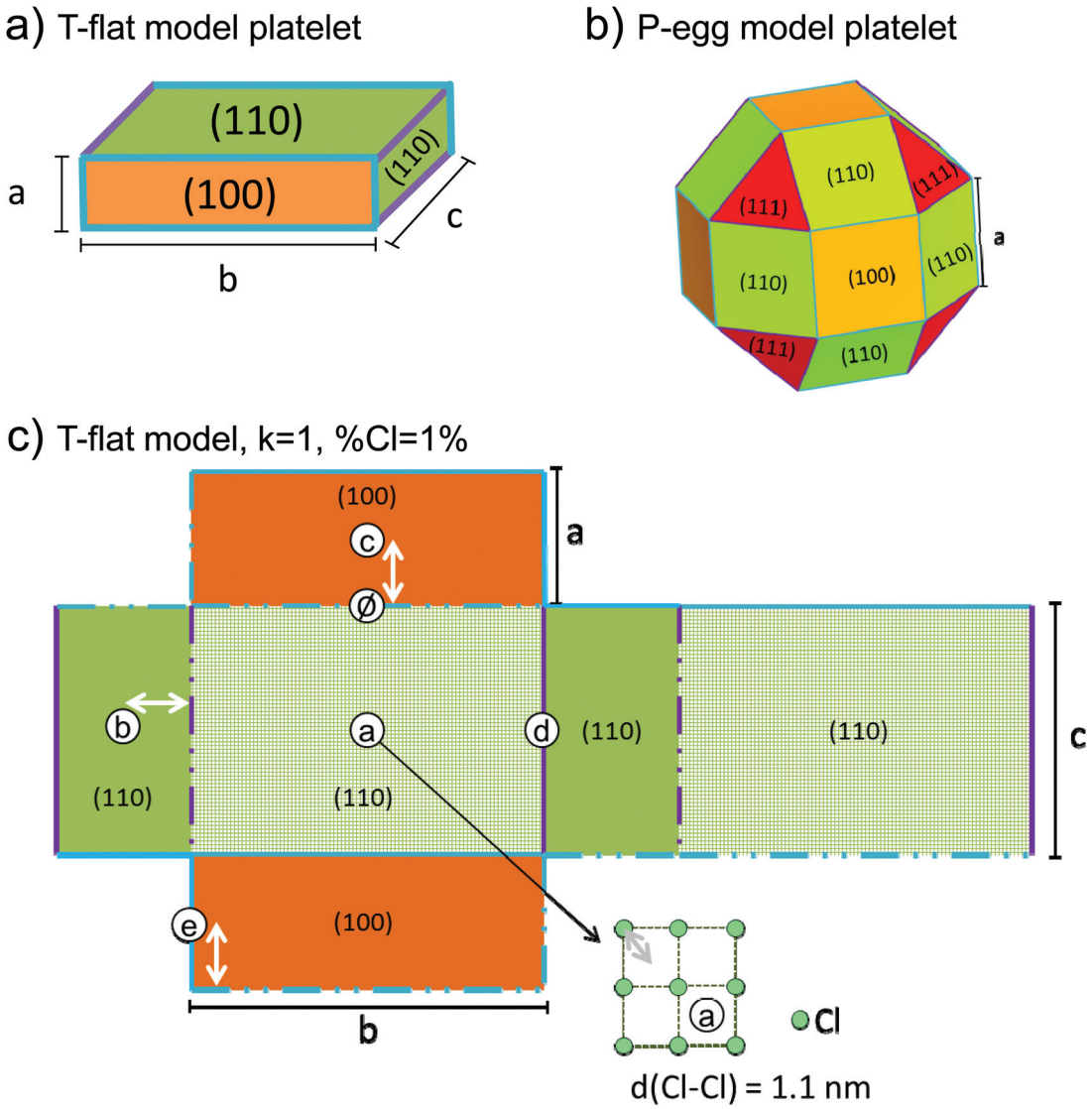

Fig. 3 Scheme of platelet model morphology for T-flat (a) and P-egg (b), showing how surface types were allocated, (110) – green, (100) – orange, (111) – red, and distinguishing the types of edge present, blue – (110)–(100) edge and purple – other edges. (c) Polyhedral net of the parallelepiped platelet model of T-flat morphology for k = 1 (size factor, see text for more explanation) and %Cl = 1% with fixed Pt NP positions considered for distance estimation shown in the white icons. Chlorinated edges are depicted by broken lines, non-chlorinated edges by full lines. The white and grey arrows indicate the shortest distance between the Pt NP position in question and chlorine atoms.

ing of multiple platelets was not considered here and that surface planes are considered to be flat, without steps or kinks: hence defects are assumed to be represented by edges located at the intersection of two facets, only. First, the model platelet dimensions were set as those measured by TEM for the alumina samples.[30] This is straight forward for the T-flat model platelet, but not for P-egg's model. In that case, the harmonic average of the three dimensions obtained by TEM was set has the diameter (d) of the circumscribed circle of the octagon that constitutes the base of the central octagonal prism, thus deriving a.

With these dimensions, geometric parameters can be calculated, such as surface area. Also, for a given %Pt and %Cl loading, Pt and Cl coverages (X nm^{-2}) as well as the number of Cl atoms and of Pt NPs per platelets can be obtained according to the equation reported in ESI section 3.† To calculate the number of Pt NPs per platelet and thus validate the model, all deposited Pt atoms are considered to be in the form of Pt_{13} NPs.

The chlorine loading at which edge anchoring sites are saturated can also be calculated: our previous work[30] showed that hydroxyls on the Al side of the (110)–(100) edge model are the most favorable to be exchanged with chlorine. Thus half the (110)–(100) edge length was used, and the distance between consecutive Cl atoms on the edge is about 0.44 nm. These parameters are detailed in Table 1.

The calculated surface areas are 221 m^2 g^{-1} and 215 m^2 g^{-1} respectively for P-egg and T-flat, in reasonable agreement with

experimental S_{BET} obtained for the samples (183 $m^2\ g^{-1}$ and 149 $m^2\ g^{-1}$, for P-egg and T-flat, respectively). The calculated values are higher than the experimental ones because only non-interacting platelets are considered here, and thus crystallite size/shape heterogeneities and stacking are not taken into account. The trend of $S_{P\text{-egg}} > S_{T\text{-flat}}$ is however maintained. Also, calculated Pt and Cl coverages (X nm^{-2}) are in the same ranges as those obtained for the prepared catalysts (Tables S2 and S3†). The number of Pt_{13} NPs per platelet also reflects the trend observed by STEM:[29] at 0.3%Pt, one or less than one particle is present by alumina platelet, thus the inter-NP distance is inter-crystallite, but it becomes intra-crystallite for higher loadings (up to 5 NP per platelet for the 1%Pt case, supported on T-flat). Finally, the calculated chlorine loading (% w/w Cl) at which the edge anchoring sites are saturated is also in agreement with our experimental NMR results,[30] which suggested that chlorine is located exclusively at edges for up to 1.4%Cl in the case of P-egg and for up to 0.5%Cl for T-flat. The platelet geometric models are thus validated and can be used to estimate inter-site distances.

To estimate the distance between acid and metallic sites the following basic hypothesis is applied: the distance is evaluated between Cl atoms and a Pt entity. This Pt entity may as well represent NPs or SAs, assuming they behave in the same way in regard to their preferential location on the platelets. For clarity, this generic Pt entity will be noted "Pt NP" in the following.

It is understood that the acid sites involved in reaction mechanisms are alumina hydroxyls with sufficient Brønsted acidity enhanced by chlorine. It is thus considered that such acidic sites are under the influence of Cl and thus in its close proximity, so Cl location can be considered as a proxy for acid site location. Indeed, in weak acidic supports such as halogenated aluminas the characterization of Brønsted acidity is difficult, as is pinpointing which of the many OH on the support have the capacity to act as acid sites.

Inter-site distances where estimated using a discrete method of calculation. For a given chlorine loading (%Cl), the shortest Pt_{NP}–Cl distance is calculated for a given Pt NP position. This is repeated for several non-equivalent Pt NP positions. These positions are either facet or edge positions. An average Pt_{NP}–Cl distance for facet or edge Pt NP positions is calculated by weighting the distances corresponding to which non-equivalent position with its exposition proportion. Global average Pt_{NP}–Cl distance, for a given %Cl, is calculated by weighting the edge and facet position averages with the proportion found by tomography for preferential Pt NP location (78% for edge positions and 22% for facet positions).[29] In absence of more information, we assume the same distribution for Pt SA. By considering the shortest possible distance in a discrete way the platinum loading (%Pt) is not a parameter in the geometrical model.

This method was applied to both platelet models for varying chlorine loading. Also, for each platelet model, three platelet sizes were considered, obtained by multiplying the model's dimensions (a, b and c for T-flat and d for P-egg) by a size factor, k. Thus, $k = 1$ corresponds to the dimensions of Table 1 and to those closest to the real alumina crystallites of

Table 1 Geometric parameters, Pt and Cl coverages and maximum chlorine loading at which edge anchoring sites are saturated obtained for validation of the T-flat and P-egg platelet models

T-flat model platelet validation

Geometric parameters		Pt and Cl coverage			
Input		Input	Output		
a (nm)	4	**% w/w Pt**	**Pt/nm^2**	**Pt$_{13}$/nm^2**	**#Pt$_{13}$/platelet**
b (nm)	14.5	0.3	0.043	0.003	1
c (nm)	9	0.6	0.086	0.007	3
Output		1	0.145	0.011	5
Total S. area (platelet) (nm^2)	449	**% w/w Cl**	**Cl/nm^2**	**#Cl/platelet**	**%Cl@edge saturation**
Specific area ($m^2\ g^{-1}$)	215	0.1	0.08	36	0.35
Total edge length (nm)	110	1	0.808	362	
		1.4	1.136	510	

P-egg model platelet validation

Geometric parameters		Pt and Cl coverage			
Input		Input	Output		
d (nm)	6.7	**% w/w Pt**	**Pt/nm^2**	**Pt$_{13}$/nm^2**	**#Pt$_{13}$/platelet**
Output		0.3	0.042	0.003	0.5
a (nm)	2.8	0.6	0.0842	0.006	1
Total S. area (platelet) (nm^2)	166	1	0.140	0.011	2
Specific area ($m^2\ g^{-1}$)	221	**% w/w Cl**	**Cl/nm^2**	**#Cl/platelet**	**%Cl@edge saturation**
Total edge length (nm)	133	0.1	0.078	13	1.20
		1	0.785	130	
		1.4	1.104	183	

our samples. k = 0.5 and k = 1.5 allow us to explore the impact of smaller and respectively larger platelet size on the inter-site distance at iso-morphology and iso-proportions. The geometric parameters for each platelet morphology and size factor are detailed in Table 2.

The edge lengths and total surface areas are interesting parameters to analyze because they provide an estimate in terms of edge site proportion for the two samples considering previous DFT models. The DFT surface models[53] exhibit a surface concentration of Al atoms of ~0.11 atom per Å^2, while the recent DFT edge models reveal a linear density of Al atoms of ~0.23 atom per Å. Considering the total surface areas and edge lengths reported in Table 2 for the two samples for k = 1, we could deduce the proportion of Al edge sites evaluated by $Al_{edge}/(Al_{edge} + Al_{surface})$ which is ~0.05 on the T-flat alumina, while it is almost 3 times higher (~0.14) for the P-egg alumina. Considering the various size factors, k, Fig. 4 shows the linear increase of the proportion of edge sites with the increase of specific area for the two samples. Obviously, the P-egg sample exhibits a larger slope than the T-flat one. Since edge sites could be the primary location for chlorine atoms,[30] this trend illustrates the impact of morphologies on chlorine location for the two samples.

To further quantify it, we consider first the T-flat alumina support, for size factor k = 1 and for a chlorine loading of 1% to exemplify the methodology detailed above. The repartition of Cl for this configuration and the Pt NP fixed positions considered are shown in Fig. 3c. In this case, the edge sites are saturated with chlorine (using half the edge length as detailed in ref. 30), some chlorine atoms must be anchored on the surface sites. After the edge sites, now saturated, the most favorable anchoring site for Cl is a AI_{IV}–μ_1-OH on the (110) facet when considering a 12.0 OH per nm^2, according to our previous DFT study.[30] This μ_1^{exch}-OH is present in the (110) facet with a density of 1.48 μ_1^{exch}-OH per nm^2, which is

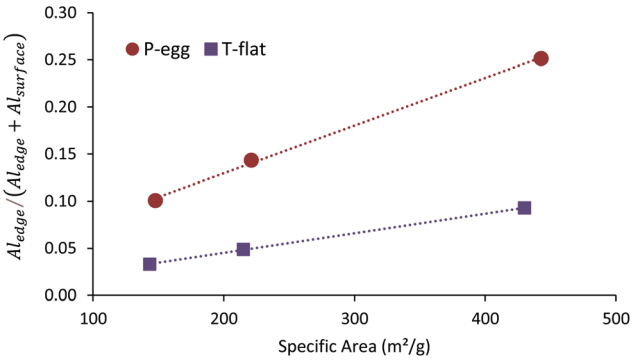

Fig. 4 Evolution of the proportion of Al edge sites with the specific area for the two alumina samples. The square and circle symbols correspond to specific areas calculated for the three size factor values (k).

Table 2 Geometric parameters for each platelet morphology, T-flat or P-egg, for the three platelet sizes considered for inter-site distance calculations. Note that k = 1 corresponds to the dimensions used to validate the platelet models, which are closest to those of the experimental catalysts' crystallites

k = 0.5			
T-flat		P-egg	
a (nm)	2	d (nm)	3.4
b (nm)	7.3	a (nm)	1.4
c (nm)	4.5		
Total S. area (platelet) (nm^2)	112	Total S. area (platelet) (nm^2)	42
Specific area (m^2 g^{-1})	430	Specific area (m^2 g^{-1})	443
Total edge length (nm)	55	Total edge length (nm)	67
k = 1			
T-flat		P-egg	
a (nm)	4	d (nm)	6.7
b (nm)	14.5	a (nm)	2.8
c (nm)	9		
Total S. area (platelet) (nm^2)	449	Total S. area (platelet) (nm^2)	166
Specific area (m^2 g^{-1})	215	Specific area (m^2 g^{-1})	221
Total edge length (nm)	110	Total edge length (nm)	133
k = 1.5			
T-flat		P-egg	
a (nm)	6	d (nm)	10.1
b (nm)	21.75	a (nm)	4.2
c (nm)	13.5		
Total S. area (platelet) (nm^2)	1010	Total S. area (platelet) (nm^2)	374
Specific area (m^2 g^{-1})	143	Specific area (m^2 g^{-1})	148
Total edge length (nm)	165	Total edge length (nm)	200

high enough to harbor all the "extra" Cl atoms needed. It is then considered that those Cl atoms are located on the basal (110) planes, uniformly distributed in a square network resulting in a Cl–Cl distance on the facet of 1.1 nm. The Pt_{NP}–Cl distance for the Pt NP fixed location (a) was then calculated by positioning the NP in the center of a Cl network square. The fixed Pt NP position ∅ corresponds to the specific case of a platinum particle located at the chlorinated edge, in which the shortest Pt–Cl distance corresponds to the Pt–Cl bond length obtained by DFT calculations as previously published[29] (Table S4,† configuration A). The position (d) is another special case in which Pt sits on an edge which is adjacent to a chlorinated surface. This distance was obtained from configuration B previously reported[29] (Table S4,† configuration B). The Pt NP–Cl distances for the other fixed positions are indicated in Fig. 3c. The complete tally of distances, the averages for surface and edge sites and global average are detailed in Table 3.

The same method was applied to both platelet morphologies, all three size factors, k, and different chlorine loadings. The equivalents of Table 3 and Fig. 3c for each case and %Cl are presented in the ESI sections 5 and 6.† These data were used to identify the parameters which influence the inter-site distance in the most significant manner.

Let us now consider the specific case of the chlorine loading at which the edge anchoring sites are saturated, meaning the chlorine loading at which all Cl atoms "fit" on edge anchoring sites only. Fig. 5 presents the %Cl at edge saturation for each platelet morphology and size, as well as the corresponding inter-site distance.

Firstly, the inter-site distances obtained for T-flat morphology are always larger than for P-egg: 1.6–4.5 nm *versus* 0.5–1.3 nm respectively. These discrepancies are significant. But the Pt NP–Cl distance for a Pt NP position on a chlorinated edge is always the same (position ∅ on the example above, of 0.23 nm). This difference is thus explained by the contribution of inter-site distances for Pt NP positions on the facets and on non-chlorinated edges to the global average. These are an expression of the platelet morphology and dimensions of the platelets: T-flat platelets have larger facets and longer edges than P-egg, at any given k, due to its more elongated morphology.

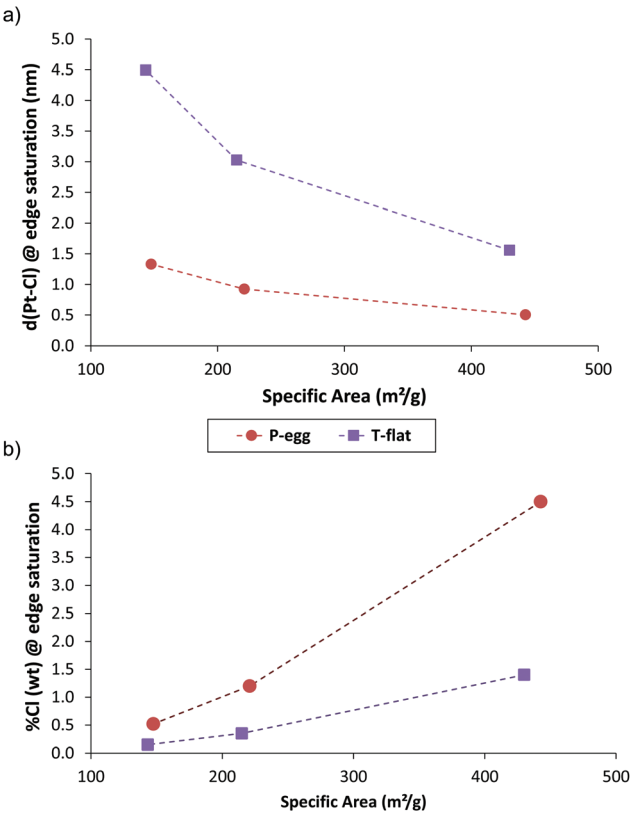

Fig. 5 (a) Inter site distance at the %Cl corresponding to edge site saturation as a function of the specific area of the model platelets; (b) chlorine loading (%Cl) corresponding to edge site saturation as a function of the specific area of the model platelets.

Table 3 Estimation of Pt NP-Cl distances for the exemplified case of T-flat, k = 1, at 1% Cl loading

Pt NP fixed position	Distance PtNP-Cl (nm)	Exposition proportion
Surface positions		
(a)	0.74	0.58
(b)	2	0.16
(c)	2	0.26
Surface average distance(nm) = $\sum_{i=\text{Surface Positions}}$ Dist. PtNP − Cl_i × Exp. proportion_i	0.74 × 0.58 + 2 × 0.16 + 2 × 0.26 = 1.27	
Edge positions		
∅	0.23	0.50
(d)	0.9	0.43
(e)	2	0.07
Edge average distance(nm) = $\sum_{i=\text{Edge Positions}}$ Dist. PtNP − Cl_j × Exp. proportion_j	0.23 × 0.5 + 0.9 × 0.43 + 2 × 0.07 = 0.65	
Global average distance (nm) = Surface average distance × Proportion of NPs on facets + Edge average distance × Proportion of NPs on edges	1.27 × 0.22 + 0.65 × 0.78 = 0.78	

Secondly, the %Cl at edge saturation is always higher for P-egg than for T-flat, for a given size factor: 0.5 *vs.* 0.15% Cl for $k = 0.5$, 4.5%Cl *vs.* 1.4%Cl for $k = 1.5$, respectively. As explained earlier and illustrated on Fig. 4, its morphology has a higher edge/surface ratio than T-flat which results in more Cl atoms that can be accommodated on the edge sites. These trends are again significantly different. Considering the case of reforming catalysts for which the %Cl is usually around 1, these results imply that a P-egg support (with specific surface area of ~200 $m^2\ g^{-1}$ for $k = 1$) is close to the edge saturation by chlorine and a minority of Cl atoms should be located on its facets. By contrast, a T-flat support (with the same specific surface area) largely exceeds the edge saturation by chlorine and thus a significant amount of chlorine (~0.65 wt% Cl) would also be present on its facets.

Let us consider now all the chlorine loadings used for distance calculations for each morphology and factor size k, as shown in Fig. 6. We observe that the average inter-site distance decreases from 5–6 nm to about 1 nm with increasing Cl loading, for both morphologies and for all k sizes. Also, the average distance decreases sharply and stagnates at about 1 nm for Cl loadings greater than that corresponding to edge site saturation with Cl atoms. This sharp decrease is more noticeable for T-flat, but the plateau after saturation is of about 1 nm for both morphologies. After the edge sites are saturated with Cl, subsequent Cl atoms must be anchored on the facets (as described in the example above) which results in the inter-site distance for Pt NP fixed positions on chlorinated facets and on non-chlorinated edges adjacent to chlorinated facets to be reduced. As a consequence, the impact of platelet morphology and/or size on inter-site distances is leveled for Cl loadings higher than that corresponding to edge saturation. Secondly, inter-site average distances are higher for T-flat than for P-egg (at a given %Cl inferior to the edge saturation loading, and a given k) because T-flat exhibits larger facets than P-egg.

If we now consider the case of reforming catalysts (1 wt% Cl and ~200 $m^2\ g^{-1}$ $k = 1$), the global average inter-site distances do not strongly depend on the two supports morphologies because both are already reaching the ~1 nm plateau. This may explain why recently reported experimental results showed that the impact of morphology is less predominant than chlorine contents on reforming catalytic activities and selectivities.[26]

If one aims at preparing two reforming catalysts with differing inter-site distances, our geometric model suggests two possibilities. On the one hand, one could synthesize each support at 1%Cl with distinct specific areas: for instance, T-flat with specific area of 400 $m^2\ g^{-1}$ leads to Pt NP–Cl of ~2 nm, while P-egg with specific area of 200 $m^2\ g^{-1}$ leads to Pt NP–Cl of ~1 nm. On the other hand, the chlorine content could be adjusted so that two supports of distinct morphology with approximately the same surface area/size exhibit precisely edge saturation by chlorine (as illustrated in Fig. 5a). In this latter case, the inter-site distances may differ by ~2 nm on the two supports with a specific area of ~200 $m^2\ g^{-1}$. Note that this proposal concerns inter-site distance only and does not take into account the variation of intrinsic strength of Brønsted acid sites with their location.

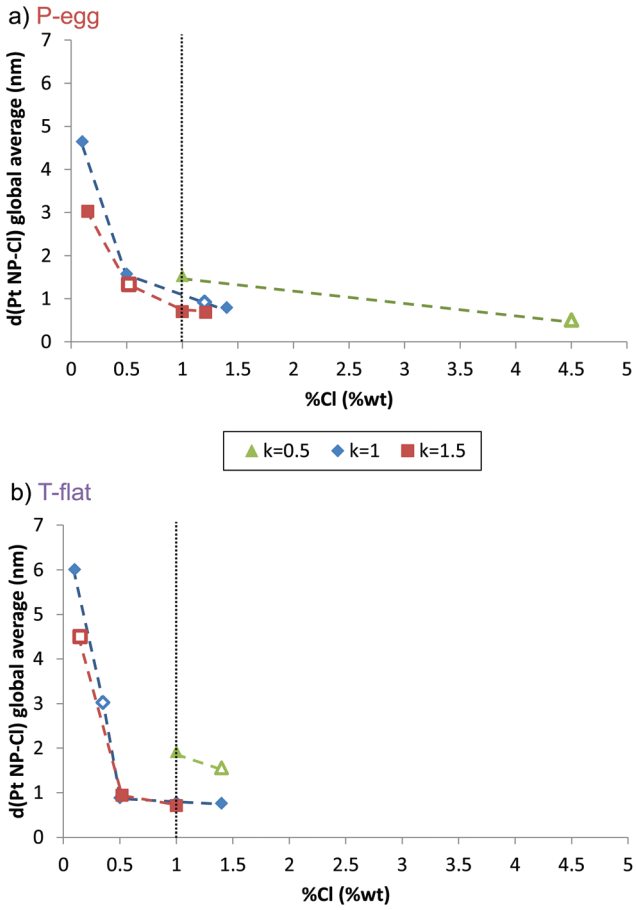

Fig. 6 Inter-site distance (global average) for (a) P-egg and (b) T-flat platelet morphologies in function of chlorine loading (%Cl) for the three k values. The points corresponding to edge saturation are identified by the empty symbol and the vertical broken lines highlight the typical Cl loading (1 wt%) used in naphtha reforming catalysts.

4. Conclusions

Sub-nanometric platinum particles supported on chlorinated γ-Al_2O_3 are bifunctional catalysts of high relevance in industry. Their characterization is made difficult by the very small size of the particles and the numerous support surface sites likely to host platinum or chlorine, whose population is tuned by the morphology of the support platelet. Gaining knowledge on the distance between the metallic and the acidic functions is a challenging prerequisite for further investigation of the parameters affecting the catalytic properties. For other better characterized bifunctional systems such as metal–zeolite systems, the distance between the two functions is often highly influential in terms of selectivity for hydrocarbon transformation reactions.

In the present work, using HR HAADF-STEM, we provided a detailed characterisation of the metallic phase features for a set of Pt/γ-Al_2O_3–Cl samples prepared by impregnation and reduction, tuning the platinum and chlorine loadings, and the morphology of the support (P-egg *versus* T-flat). All samples exhibit similar particle size distribution, with an average diameter of 0.9 nm and similar shape of biplanar clusters. Thus, the platinum content affects only the particle concentration and not their size nor shape, whereas chlorine loadings and support morphology do not affect these parameters significantly. Conversely, the proportion of single atoms, present on all samples, was shown to be mainly affected by chlorine loading and support morphology: the higher the chlorine and the edge/defect contents at the support, the higher the concentration of single atoms.

With such data in hand, combined with previously obtained knowledge[29,30] about the location of chlorine and of the particles on the support (both in majority at the edges of the platelets), we were able to propose geometric model of Pt/alumina-Cl catalysts, making a significant distinction between the two support morphologies. From these models, the dependance of average inter-site distance was quantitatively analyzed by considering three key physico-chemical parameters: the chlorine loading, the morphology of the support, and the platelet size (correlated to specific area) for a given morphology. The predicted inter-site distance ranges from less than 1 nm to more than 6 nm. Inter-site distance decreases with increasing chlorine loading. Platelet morphology has two impacts: on the one hand larger facets lead to larger inter-site distances, on the other hand a higher edge to surface ratio results in a higher chlorine loading at which edge sites are saturated. However, the impact of support morphology on inter-site distance is revealed only for chlorine contents smaller or equal to edge saturation. We discussed how these parameters may impact the properties of naphtha reforming catalyst.

In the future, it would be welcome to include explicitly in our geometrical model the effect of SA on the inter-site distance. For that purpose, it will be needed to characterize their precise location on the alumina particles (proportion at edge and facet) as we recently undertook for Pt NP.[29] Also, a finer spectroscopic characterization of the weak Brønsted acid sites (strength and location) promoted by chlorine on alumina by the use of specific basic probe molecules[20] would be valuable to further improve our model.

More generally, such predictions may open the door to the better understanding of the catalytic properties of the Pt/γ-Al_2O_3–Cl catalysts families. Also, they are likely transposable to many other families of bifunctional catalysts involving oxide supported metallic nanoparticles.

Author contributions

ATFB, CC and PR are credited with writing the original draft. ATFB and A-LT are credited with investigation. ATFB is credited with visualization. CC, FD, A-SG, and PR are credited with conceptualization, project administration, resources, supervision, validation, and review & editing. OE is credited with project administration, resources, validation, and review & editing.

All authors have given approval to the final version of the manuscript.

Conflicts of interest

There are no conflicts to declare.

Acknowledgements

This work was funded by IFPEN and supported by the LCR "CARactérisation des Matériaux pour l'Energie" (CARMEN). E. Rosati is acknowledged for preparing the support extrudates. C. Voisin and C. Guégan are acknowledged for technical assistance for catalysts preparation.

References

1 C. Marcilly, in *Acido-basic catalysis*, ed. C. Marcilly, Editions Technip, Paris, 2006.
2 *Catalysis by transition metal sulphides. From molecular theory to industrial application*, ed. H. Toulhoat and P. Raybaud, Ed. Technip, Paris, 2013.
3 J. H. Sinfelt, Bifunctional Catalysis, *Adv. Chem. Eng.*, 1964, **5**, 37–74.
4 H. L. Coonradt and W. E. Garwood, Mechanism of Hydrocracking. Reactions of Paraffins and Olefins, *Ind. Eng. Chem. Process Des. Dev.*, 1964, **3**, 38–45.
5 P. B. Weisz, Polyfunctional Heterogeneous Catalysis, *Adv. Catal.*, 1962, **13**, 137–190.
6 M. Guisnet, "Ideal" bifunctional catalysis over Pt-acid zeolites, *Catal. Today*, 2013, **218–219**, 123–134.
7 N. Batalha, L. Pinard, C. Bouchy, E. Guillon and M. Guisnet, n-Hexadecane hydroisomerization over Pt-HBEA catalysts. Quantification and effect of the intimacy between metal and protonic sites, *J. Catal.*, 2013, **307**, 122–131.
8 J. E. Samad, J. Blanchard, C. Sayag, C. Louis and J. R. Regalbuto, The controlled synthesis of metal-acid bifunctional catalysts: Selective Pt deposition and nanoparticle synthesis on amorphous aluminosilicates, *J. Catal.*, 2016, **342**, 213–225.
9 E. Gutierrez-Acebo, C. Leroux, C. Chizallet, Y. Schuurman and C. Bouchy, Metal/Acid Bifunctional Catalysis and Intimacy Criterion for Ethylcyclohexane Hydroconversion: When Proximity Does Not Matter, *ACS Catal.*, 2018, **8**, 6035–6046.
10 P. S. F. Mendes, J. M. Silva, M. F. Ribeiro, P. Duchêne, A. Daudin and C. Bouchy, Quantification of metal-acid balance in hydroisomerization catalysts, *AIChE J.*, 2017, **63**, 2864–2875.

11 J. Zečević, G. Vanbutsele, K. P. de Jong and J. A. Martens, Nanoscale intimacy in bifunctional catalysts for selective conversion of hydrocarbons, *Nature*, 2015, **528**, 245–248.
12 J. Oenema, J. Harmel, R. P. Vélez, M. J. Meijerink, W. Eijsvogel, A. Poursaeidesfahani, T. J. H. Vlugt, J. Zečević and K. P. de Jong, Influence of Nanoscale Intimacy and Zeolite Micropore Size on the Performance of Bifunctional Catalysts for n-Heptane Hydroisomerization, *ACS Catal.*, 2020, **10**, 14245–14257.
13 P. S. F. Mendes, J. M. Silva, M. Filipa Ribeiro, A. Daudin and C. Bouchy, From powder to extrudate zeolite-based bifunctional hydroisomerization catalysts: on preserving zeolite integrity and optimizing Pt location, *J. Ind. Eng. Chem.*, 2018, **62**, 72–83.
14 P. Avenier, D. Bazer-Bachi, F. Bazer-Bachi, C. Chizallet, F. Deleau, F. Diehl, J. Gornay, É. Lemaire, V. Moizan-Basle, C. Plais, P. Raybaud, F. Richard and S. Lacombe, Catalytic Reforming: Methodology and Process Development for a Constant Optimisation and Performance Enhancement, *Oil Gas Sci. Technol. – Rev. IFP Energies nouvelles*, 2016, **71**, 41.
15 P.-Y. le Goff, W. Kostka and J. Ross, in *Springer Handbook of Petroleum Technology*, Springer, New York, 2nd edn, 2017, pp. 589–616.
16 J. Zhang, Y.-T. Tsai, K. L. Sangkaewwattana and J. Goodwin, Structure sensitivity of cyclopropane hydrogenolysis on carbon-supported platinum, *J. Catal.*, 2011, **280**, 89–95.
17 B. H. Davis, Alkane dehydrocyclization mechanism, *Catal. Today*, 1999, **53**, 443–516.
18 A. Gallo, A. Fong, K. C. Szeto, J. Rieb, L. Delevoye, R. M. Gauvin, M. Taoufik, B. Peters and S. L. Scott, Ligand Exchange-Mediated Activation and Stabilization of a Re-Based Olefin Metathesis Catalyst by Chlorinated Alumina, *J. Am. Chem. Soc.*, 2016, **138**, 12935–12947.
19 G. Busca, Spectroscopic characterization of the acid properties of metal oxide catalysts, *Catal. Today*, 1998, **41**, 191–206.
20 Q. Rivet, J. Meyet, M. Rivallan, T. Nardin and D. Farrusseng, Characterization of the Brønsted acidity of $PtSn/Al_2O_3$ surfaces by adsorption of 2,6-di-tert-butylpyridine, *New J. Chem.*, 2022, **46**, 7557–7562.
21 N. B. Muddada, U. Olsbye, T. Fuglerud, S. Vidotto, A. Marsella, S. Bordiga, D. Gianolio, G. Leofanti and C. Lamberti, The role of chlorine and additives on the density and strength of Lewis and Brønsted acidic sites of γ-Al_2O_3 support used in oxychlorination catalysis: A FTIR study, *J. Catal.*, 2011, **284**, 236–246.
22 M. Digne, P. Raybaud, P. Sautet, D. Guillaume and H. Toulhoat, Atomic scale insights on chlorinated gamma-alumina surfaces, *J. Am. Chem. Soc.*, 2008, **130**, 11030–11039.
23 P. Berteau, M.-A. Kellens and B. Delmon, Acid-Base Properties of Modified Aluminas, *J. Chem. Soc., Faraday Trans.*, 1991, **87**, 1425–1431.
24 G. Clet, J. Goupil, G. Szabo and D. Cornet, Chlorinated alumina as an alkylation catalyst: influence of superficial HCl, *J. Mol. Catal. A: Chem.*, 1999, **148**, 253–264.
25 O. Said-Aizpuru, A. T. F. Batista, C. Bouchy, V. Petrazzuoli, F. Allain, F. Diehl, D. Farrusseng, F. Morfin, J.-F. Joly and A. Dandeu, Non monotonous product distribution dependence on Pt/γ–Al_2O_3–Cl catalysts formulation in n–heptane reforming, *ChemCatChem*, 2020, **12**, 2262–2270.
26 O. Said-Aizpuru, F. Allain, A. Dandeu, F. Diehl, D. Farrusseng and J.-F. Joly, Kinetic modelling of Pt/γ-Al_2O_3–Cl catalysts formulation changes in n-heptane reforming, *React. Chem. Eng.*, 2021, **6**, 1079–1091.
27 O. Said-Aizpuru, F. Allain, F. Diehl, D. Farrusseng, J.-F. Joly and A. Dandeu, A naphtha reforming process development methodology based on the identification of catalytic reactivity descriptors, *New J. Chem.*, 2020, **44**, 7243–7260.
28 P. Raybaud, C. Chizallet, C. Mager-Maury, M. Digne, H. Toulhoat and P. Sautet, From γ-alumina to supported platinum nanoclusters in reforming conditions, *J. Catal.*, 2013, **308**, 328–340.
29 A. T. F. Batista, W. Baaziz, A.-L. Taleb, J. Chaniot, M. Moreaud, C. Legens, A. Aguilar-Tapia, O. Proux, J.-L. Hazemann, F. Diehl, C. Chizallet, A.-S. Gay, O. Ersen and P. Raybaud, Atomic Scale Insight into the Formation, Size, and Location of Platinum Nanoparticles Supported on γ-Alumina, *ACS Catal.*, 2020, **10**, 4193–4204.
30 A. T. F. Batista, D. Wisser, T. Pigeon, D. Gajan, F. Diehl, M. Rivallan, L. Catita, A.-S. Gay, A. Lesage, C. Chizallet and P. Raybaud, Beyond gamma-Al_2O_3 crystallite surfaces: the hidden features of Edges revealed by Solid-State ^{1}H NMR and DFT calculations, *J. Catal.*, 2019, **378**, 140–143.
31 A. Wang, J. Li and T. Zhang, Heterogeneous single-atom catalysis, *Nat. Rev. Chem.*, 2018, **2**, 65–81.
32 X. Cui, W. Li, P. Ryabchuk, K. Junge and M. Beller, Bridging homogeneous and heterogeneous catalysis by heterogeneous single-metal-site catalysts, *Nat. Catal.*, 2018, **1**, 385–397.
33 J. Liu, Catalysis by Supported Single Metal Atoms, *ACS Catal.*, 2017, **7**, 34–59.
34 L. Piccolo, Restructuring effects of the chemical environment in metal nanocatalysis and single-atom catalysis, *Catal. Today*, 2021, **373**, 80–97.
35 R. Lang, X. Du, Y. Huang, X. Jiang, Q. Zhang, Y. Guo, K. Liu, B. Qiao, A. Wang and T. Zhang, Single-Atom Catalysts Based on the Metal-Oxide Interaction, *Chem. Rev.*, 2020, **120**, 11986–12043.
36 S. K. Kaiser, Z. Chen, D. Faust Akl, S. Mitchell and J. Pérez-Ramírez, Single-Atom Catalysts across the Periodic Table, *Chem. Rev.*, 2020, **120**, 11703–11809.
37 M. Moses-DeBusk, M. Yoon, L. F. Allard, D. R. Mullins, Z. Wu, X. Yang, G. Veith, G. M. Stocks and C. K. Narula, CO Oxidation on Supported Single Pt Atoms: Experimental and ab Initio Density Functional Studies of CO Interaction with Pt Atom on θ-Al_2O_3(010) Surface, *J. Am. Chem. Soc.*, 2013, **135**, 12634–12645.
38 X. Cui, K. Junge, X. Dai, C. Kreyenschulte, M.-M. Pohl, S. Wohlrab, F. Shi, A. Brückner and M. Beller, Synthesis of Single Atom Based Heterogeneous Platinum Catalysts:

High Selectivity and Activity for Hydrosilylation Reactions, *ACS Cent. Sci.*, 2017, **3**, 580–585.

39 C. Dessal, A. Sangnier, C. Chizallet, C. Dujardin, F. Morfin, J.-L. Rousset, M. Aouine, M. Bugnet, P. Afanasiev and L. Piccolo, Atmosphere-dependent stability and mobility of catalytic Pt single atoms and clusters on γ-Al_2O_3, *Nanoscale*, 2019, **11**, 6897–6904.

40 C. Dessal, T. Len, F. Morfin, J.-L. Rousset, M. Aouine, P. Afanasiev and L. Piccolo, Dynamics of Single Pt Atoms on Alumina during CO Oxidation Monitored by Operando X-ray and Infrared Spectroscopies, *ACS Catal.*, 2019, **9**, 5752–5759.

41 A. M. Gänzler, M. Casapu, P. Vernoux, S. Loridant, F. J. Cadete Santos Aires, T. Epicier, B. Betz, R. Hoyer and J.-D. Grunwaldt, Tuning the Structure of Platinum Particles on Ceria In Situ for Enhancing the Catalytic Performance of Exhaust Gas Catalysts, *Angew. Chem., Int. Ed.*, 2017, **56**, 13078–13082.

42 G. Lietz, H. Lieske, H. Spindler, W. Hanke and J. Völter, Reactions of platinum in oxygen- and hydrogen-treated Ptγ-Al_2O_3 catalysts: II. Ultraviolet-visible studies, sintering of platinum, and soluble platinum, *J. Catal.*, 1983, **81**, 17–25.

43 N. S. Guyot-Sionnest, F. Villain, D. Bazin, H. Dexpert, F. Le Peltier, J. Lynch and J. P. Bournonville, In situ high temperature and high pressure EXAFS studie of Pt/Al_2O_3 catalysts. Part I: Reduction and deactivation, *Catal. Lett.*, 1991, **8**, 283–295.

44 J. Lynch, Development of Structural Characterisation Tools for Catalysts, *Oil Gas Sci. Technol.*, 2002, **57**, 281–305.

45 F. Le Normand, A. Borgna, T. F. Garetto, C. R. Apesteguia and B. Moraweck, Redispersion of Sintered Pt/Al_2O_3 Naphtha Reforming Catalysts: An in Situ Study Monitored by X-ray Absorption Spectroscopy, *J. Phys. Chem.*, 1996, **100**, 9068–9076.

46 W. Sinkler, S. I. Sanchez, S. A. Bradley, J. Wen, B. Mishra, S. D. Kelly and S. R. Bare, Aberration-Corrected Transmission Electron Microscopy and In Situ XAFS Structural Characterization of Pt/γ-Al_2O_3 Nanoparticles, *ChemCatChem*, 2015, **7**, 3779–3787.

47 J. Lee, E. J. Jang and J. H. Kwak, Effect of number and properties of specific sites on alumina surfaces for Pt-Al_2O_3 catalysts, *Appl. Catal., A*, 2019, **569**, 8–19.

48 S. A. Bradley, W. Sinkler, D. A. Blom, W. Bigelow, P. M. Voyles and L. F. Allard, Behavior of Pt Atoms on Oxide Supports During Reduction Treatments at Elevated Temperatures, Characterized by Aberration Corrected Stem Imaging, *Catal. Lett.*, 2012, **142**, 176–182.

49 M. Vaarkamp, J. T. Miller, F. S. Modica and D. C. Koningsberger, On the Relation between Particle Morphology, Structure of the Metal-Support Interface, and Catalytic Properties of Pt/γ-Al_2O_3, *J. Catal.*, 1996, **163**, 294–305.

50 C. H. Hu, C. Chizallet, C. Mager-Maury, M. Corral-Valero, P. Sautet, H. Toulhoat and P. Raybaud, Modulation of catalyst particle structure upon support hydroxylation, *J. Catal.*, 2010, **274**, 99–110.

51 C. Mager-Maury, C. Chizallet, P. Sautet and P. Raybaud, Platinum Nanoclusters Stabilized on γ-Alumina by Chlorine Used As a Capping Surface Ligand, *ACS Catal.*, 2012, **2**, 1346–1357.

52 C. Mager-Maury, G. Bonnard, C. Chizallet, P. Sautet and P. Raybaud, H_2-Induced Reconstruction of Supported Pt Clusters, *ChemCatChem*, 2011, **3**, 200–207.

53 M. Digne, P. Sautet, P. Raybaud, P. Euzen and H. Toulhoat, Use of DFT to achieve a rational understanding of acid-Basic properties of alumina surfaces, *J. Catal.*, 2004, **226**, 54–68.

54 P. Nortier, P. Fourre, A. M. Saad, O. Saur and J. C. Lavalley, Effects of crystallinity and morphology on the surface properties ofalumina, *Appl. Catal.*, 1990, **61**, 141–160.

55 L. Kovarik, A. Genç, C. Wang, J. Szanyi, C. Peden and J. Kwak, Tomography and high resolution study of gamma-Al_2O_3 porosity, surfaces and Pt surface interaction, *Microsc. Microanal.*, 2012, **18**, 1302–1303.

56 J.-P. Beaufils and Y. Barbaux, Détermination, par diffraction différentielle de neutrons, des faces cristallines exposées par des supports de catalyseurs en poudre, *J. Chim. Phys.*, 1981, **78**, 347–352.